Research Article | Vol. 15, No. 2 / 1 Feb 2024 / Biomedical Optics Express 1004
Biomedical Optics EXPRESS

Wide-field intensity fluctuation imaging

QINGWEI FANG,[1] ALANKRIT TOMAR,[2] AND ANDREW K. DUNN[1,2,*]

[1]Department of Biomedical Engineering, The University of Texas at Austin, Austin, Texas 78712, USA
[2]Department of Electrical and Computer Engineering, The University of Texas at Austin, Austin, Texas 78712, USA
*adunn@utexas.edu

Abstract: The temporal intensity fluctuations contain important information about the light source and light-medium interaction and are typically characterized by the intensity autocorrelation function, $g_2(\tau)$. The measurement of $g_2(\tau)$ is a central topic in many optical sensing applications, ranging from stellar intensity interferometer in astrophysics, to fluorescence correlation spectroscopy in biomedical sciences and blood flow measurement with dynamic light scattering. Currently, $g_2(\tau)$ at a single point is readily accessible through high-frequency sampling of the intensity signal. However, two-dimensional wide-field imaging of $g_2(\tau)$ is still limited by the cameras' frame rate. We propose and demonstrate a 2-pulse within-exposure modulation approach to break through the camera frame rate limit and obtain the quasi $g_2(\tau)$ map in wide field with cameras of only ordinary frame rates.

1. Introduction

The intensity correlation function is widely used for quantifying optical fluctuations and its measurement has great physical and physiological significance in many optical sensing applications. It was first introduced in 1956 as intensity interferometry to measure the apparent angular diameter of stars [1] and recently used to study stellar emission processes and calibrate star distances in astrophysics [2,3]. It plays an essential role in fluorescence correlation spectroscopy (FCS) in determining the diffusion coefficient of molecules and investigating biomolecular interaction processes [4–8]. It is used to achieve super-resolution optical fluctuation imaging (SOFI) [9–11]. It is used for particle sizing in dynamic light scattering [12–14]. In addition, tissue blood flow and perfusion information can be extracted from it, on which diffuse correlation spectroscopy [15–17] (DCS) and laser speckle contrast imaging [18–22] (LSCI) are developed.

Generally, the intensity autocorrelation function measures the similarity of the intensity signal with itself between now and a moment later. It is defined as $g_2(\tau) = \frac{\langle I(t)I(t+\tau)\rangle}{\langle I\rangle^2}$ where τ is the time lag, $I(t)$ is the intensity signal of interest and $\langle\ \rangle$ denotes averaging. To resolve the intensity autocorrelation function, high temporal resolution detectors, such as avalanche photodiodes (APD) or single-photon avalanche diodes (SPAD), are required to record the intensity at sufficiently high sampling rates. However, these one-dimensional detectors are only capable of single-point $g_2(\tau)$ measurements.

Light sheet or total internal reflection microscopy enables 2-dimensional (2D) FCS measurements at thousands of locations simultaneously by camera-based fluorescence intensity recording [23,24]. However, the electron multiplying charge coupled devices (EM-CCD), which are currently considered the most suitable option in comprehensive comparison with other types of 2D detectors [8,25], are still limited in frame rates ($\sim$ 1000 frames per second) and suffer from high instrumentation cost.

In DCS and LSCI, some high-speed cameras have been used to record the raw laser speckle signal and measure $g_2(\tau)$ in a 2D field of view (FOV) [26,27]. In addition, SPAD arrays are utilized by speckle contrast optical spectroscopy to create synthetic multiple-exposure speckle contrast data [28–30]. However, both methods suffer from limited field of view and high

#506870 https://doi.org/10.1364/BOE.506870
Journal © 2024 Received 25 Sep 2023; revised 8 Jan 2024; accepted 9 Jan 2024; published 24 Jan 2024

Biomedical Optics EXPRESS

instrumentation cost to resolve the signal at sufficient frame rates. Recently rolling shutters have been demonstrated helpful in alleviating the frame rate limit of cameras [31]. But the method trades the spatial resolution for temporal resolution and cannot measure $g_2(\tau)$ of slowly varying dynamics due to the limited length of elongated speckle patterns created by the elliptical aperture.

Overall, $g_2(\tau)$ is still measured based on the fully time-resolved signal, from which, however, high-frequency signal sampling is inevitable. As such, current methods must sacrifice either field of view or spatial resolution to accelerate the signal sampling. Here we propose a method to measure $g_2(\tau)$ without resolving the fast temporal dynamics of the signal, thereby enabling characterization of rapid intensity fluctuations even at low camera frame rates.

Our method borrows the idea of speckle contrast from LSCI. The relationship between speckle contrast K and $g_2(\tau)$ has been well established in LSCI, where the pixel intensity $S(T)$ is defined as

$$S(T) = \int_0^T I(t)dt. \tag{1}$$

The speckle contrast is then defined as

$$K(T) = \frac{\sigma_s}{\langle S \rangle}. \tag{2}$$

Speckle contrast can be calculated either spatially or temporally. Spatially, a $N \times N$ sliding window is typically used across the image to generate the speckle contrast of the center pixel by computing the standard deviation and mean of all N^2 pixel intensities within the window under the assumption of ergodicity [21]. Temporally, a series of images with the same camera exposure time can be acquired to calculate the speckle contrast at a certain pixel by computing the standard deviation over the mean of the pixel's intensity in those images.

Note that speckle contrast can be measured with a much lower frame rate than $g_2(\tau)$ since what it evaluates is the statistical properties of the *integrated* signal, S within the camera exposure time T. The integrated signal's speckle contrast K within different T can be measured by multiple exposures of different exposure times [32–35]. The camera exposures do not have to be consecutive or acquired with a fast frame rate as long as the statistical property of the signal remains unchanged over the multiple exposures.

Speckle contrast is related to $g_2(\tau)$ in a way that K^2 is an integral of $g_2(\tau)$ weighted by a right triangle function $(T - \tau)$ if the illumination is held constant within the camera exposure [36]

$$K^2(T) = \frac{2}{T^2} \int_0^T (T - \tau) g_2(\tau) d\tau - 1. \tag{3}$$

Recently, Siket et al. have generalized the relationship to cases where the illumination can be modulated by an arbitrary waveform [37] (Supplemental section S1), namely

$$K^2(T) = \frac{2\langle I \rangle^2}{T^2 \langle I_m \rangle^2} \int_0^T M(\tau) g_2(\tau) d\tau - 1 \tag{4}$$

where I_m is the modulated signal intensity and $I_m(t) = I(t)m(t)$ where $m(t)$ is the modulation waveform within the camera exposure and ranges from 0 to 1. $M(\tau)$ is the autocorrelation of the modulation waveform defined as $M(\tau) = \int_0^{T-\tau} m(t)m(t+\tau)dt$.

One important observation from Eq. (4) is that if we could find a modulation waveform $m(t)$ such that $K^2(T) = g_2(T)$, then we can measure $g_2(\tau = T)$ by measuring $K^2(T)$ at a much lower frame rate. We achieve this by 2-pulse modulated multiple-exposure imaging with two illumination pulses placed inside the exposure and their temporal separation varied across exposures (Fig. 1(a)). The pulse duration is denoted as T_m while the temporal separation denoted as T. Note that the T in 2-pulse modulation context is different from camera exposure time. The

Biomedical Optics EXPRESS

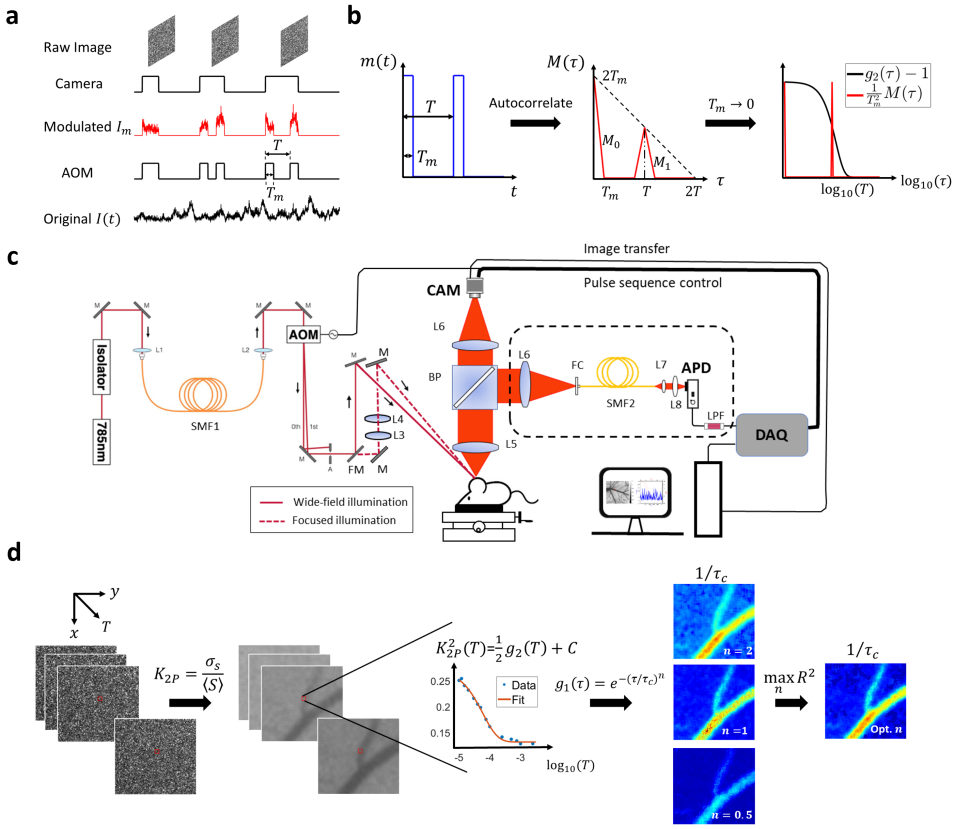

Fig. 1. Overview of the methodology and instrumentation. **a** Temporal relationship between intensity modulation and camera exposure. The x-axis is time. AOM: acousto-optic modulator. The sample is illuminated only when AOM modulation voltage is high. Hence for I_t, only the signal when AOM is high will be recorded and integrated onto the camera raw image. T: the period of the two-pulse modulation waveform. T_m: pulse duration. **b** The autocorrelation function of 2-pulse modulation waveform. $m(t)$: intensity modulation waveform. $m(t) \in [0, 1]$. $M(\tau)$: the autocorrelation of $m(t)$. $M(\tau) = \int_0^{T-\tau} m(t)m(t+\tau)dt$. $M(\tau)$ consists of two pulses denoted as M_0 and M_1. When T_m is approaching 0, $\frac{1}{T_m^2}M(\tau)$ becomes the sum of two delta functions. **c** Diagram of the instrumentation of this study. Two illumination light paths are constructed: widefield (real line) and focused (dashed line). The light is switched between the two paths by a flip mirror but modulated by the same pulse sequence. The diffusely reflected light is collected by the objective and then split by a 50/50 beamsplitter. The two splits are collected by camera and APD, respectively. AOM: acousto-optic modulator. BP: 50/50 beamsplitter plate. APD: avalanche photodiode. DAQ: data acquisition board. CAM: camera. L: lens. M: mirror. FM: flip mirror. FC: fiber coupler. SMF: single-mode fiber. LPF: low-pass filter. **d** The workflow of extracting correlation time from 2-pulse modulated multiple-exposure raw images. The 2-pulse modulated speckle contrast, K_{2P}, is first computed from the modulated raw speckle images and its trace along the third dimension T is then fitted with different electric field autocorrelation $g_1(\tau)$ models (n = 2, 1 or 0.5). The best $g_1(\tau)$ model is identified by maximizing the coefficient of determination, R^2.

Biomedical Optics EXPRESS

camera exposure now should be no shorter than $T + T_m$ to ensure that the two illumination pulses fall within the camera exposure. The two illumination pulses are created by externally modulating the laser with an acousto-optic modulator (AOM). The idea is that when the pulse duration T_m is approaching 0, $M(\tau)$ weighted by $1/T_m^2$ would become the sum of two delta functions (Fig. 1(b)) and Eq. (4) would be reduced to

$$K_{2P}^2(T) = \frac{1}{2}g_2(T) + C \tag{5}$$

where $K_{2P}^2(T)$ represents the square of the 2-pulse modulated speckle contrast and C is a constant that is independent of T (Method 2.1). Since $K_{2P}^2(T)$ forms a linear relationship with $g_2(T)$, we call it quasi $g_2(\tau)$.

Cameras of ordinary frame rates as low as 1 Hz are sufficient for our $g_2(\tau)$ measurement approach as long as the signal's statistical property remains invariant within the measurement. The camera-based characterization of $g_2(\tau)$ at various time lags is first validated against the $g_2(\tau)$ curve obtained by the traditional single-point photodiode measurement with 1 MHz sampling rate (instrumentation shown in Fig. 1(c)). Furthermore, wide-field quasi $g_2(\tau)$ measurement and correlation time mapping are demonstrated in case of *in vivo* blood flow imaging (workflow summarized in Fig. 1(d)).

2. Method

2.1. Theory

In this section, we explain why $K_{2P}^2(T) = \frac{1}{2}g_2(T) + C$ is true when the pulse duration is approaching 0 in 2-pulse modulation intuitively. The rigorous and full derivation can be found in Supplemental sections S1 and section S2. For a 2-pulse modulation waveform $m(t)$ shown in Fig. 1(b), $m(t)$ can be written as

$$m(t) = \begin{cases} 1, & t \in [0, T_m] \cup [T, T + T_m] \\ 0, & t \in (T_m, T) \cup (T + T_m, 2T] \end{cases} \tag{6}$$

where T_m is the duration of a single illumination pulse and T is the period of the modulation waveform. The duty cycle is $d = T_m/T$. In this case, Eq. (4) can be simplified to

$$K_{2P}^2(T) = \frac{1}{2T_m^2}\int_0^{2T} M(\tau)g_2(\tau)d\tau - 1 \tag{7}$$

where the subscript $2P$ denotes the speckle contrast under 2-pulse modulation. The corresponding autocorrelation function of the modulation waveform, $M(\tau)$, is a pulse train consisting of two triangle pulses $M_0(\tau)$ and $M_1(\tau)$ (Fig. 1(b)),

$$M_0(\tau) = \begin{cases} 2(T_m - \tau), & t \in [0, T_m] \\ 0, & t \in (T_m, 2T] \end{cases} \tag{8}$$

$$M_1(\tau) = \begin{cases} \tau - (T - T_m), & t \in [T - T_m, T] \\ T + T_m - \tau, & t \in (T, T + T_m] \\ 0, & t \in [0, T - T_m) \cup (T + T_m, 2T] \end{cases} \tag{9}$$

$M(\tau) = M_0(\tau) + M_1(\tau)$ and is valid for either $d <= 0.5$ or $d > 0.5$.

Note that the first right triangle pulse $M_0(\tau)$ is solely dependent on T_m and independent of the temporal separation of the two illumination pulses T. In addition, the shape of $M_1(\tau)$, specifically the width and height, is independent of T too. The horizontal position of $M_1(\tau)$, however depends on T. Therefore, when T is varied while holding T_m constant, the second triangle pulse $M_1(\tau)$

Biomedical Optics EXPRESS

will move horizontally. Since $K_{2P}^2(T)$ is the integral of the product of $M(\tau)$ and $g_2(\tau)$, the second triangle pulse, $M_1(\tau)$, sweeps the $g_2(\tau)$ curve as T changes, through which selective sampling of the $g_2(\tau)$ curve is achieved.

Scaling $M(\tau)$ by $1/T_m^2$ as in Eq. (7), we find that the height/width ratio of its two triangle pulses increases as the illumination pulse duration T_m decreases. In the special case where T_m approaches 0, $M(\tau)$ weighted by $\frac{1}{T_m^2}$ becomes the sum of two delta functions

$$\lim_{T_m \to 0} \frac{1}{T_m^2} M(\tau) = \delta(0) + \delta(T) \tag{10}$$

Therefore, Eq. (7) simplifies to Eq. (5) where C is a constant representing the contribution of $M_0(\tau)$ which is independent of T. Specifically, $C = \frac{1}{2} g_2(0) - 1$ when the impact of T_m on C is negligible. A rigorous proof and full derivation of Eq. (5) in this case from the perspective of statistics can be found in Supplemental section S2. Note that this supplemental proof is valid without assuming Eq. (3), (4) or (7). When T_m must be accounted for, $C = \frac{1}{T_m^2} \int_0^{T_m} (T_m - \tau) g_2(\tau) d\tau - 1$. C can also be estimated from the $K_{2P}^2(T)$ curve since $C = \lim_{T \to \infty} K_{2P}^2(T) - 0.5$ if $g_2(\tau)$ decreases to 1 when τ is infinitely large. Removing the constant C and the scaling factor $\frac{1}{2}$ in Eq. (5) through normalization, we have

$$\widetilde{K_{2P}^2(T)} = \widetilde{g_2}(T) \tag{11}$$

where $\widetilde{X}$ represents the normalization of X, i.e. $\widetilde{X} = \frac{X - \min(X)}{\max(X) - \min(X)}$.

As a secondary topic, to address the engineering issues of implementing 2-pulse modulation using an AOM of limited contrast ratio, we modeled the non-zero residual illumination between the two illumination pulses and provided a detailed theoretical analysis in Supplemental section 3. It is placed in Supplemental document to focus the main text in the core 2-pulse modulation idea. But we encourage readers to look for more details there if they are interested in the rigorous theory behind it.

2.2. Numerical simulation

For any given $g_2(\tau)$ curve, the 2-pulse modulated $K_{2P}^2(T)$ can be simulated according to Eq. (7). For the same $g_2(\tau)$ curve, the corresponding traditional $K^2(T)$ without modulation can be simulated according to Eq. (3).

Particularly, when $g_2(\tau)$ assumes the following form,

$$g_2(\tau) = 1 + \beta[\rho e^{-\tau/\tau_c} + (1 - \rho)]^2 + v_n \tag{12}$$

the analytical solution of the corresponding speckle contrast in the 2-pulse modulation without any approximation would be

$$K_{2P}^2(T) = \frac{1}{2T_m^2}[2\widetilde{B}(T_m) + \widetilde{B}(T - T_m) + \widetilde{B}(T + T_m) - 2\widetilde{B}(T)] + \beta(1 - \rho^2) + v_n \tag{13}$$

where $\widetilde{B}(\tau) = \frac{1}{4}\tau_c^2 \beta \rho^2 [e^{-2x} - 1 + 2x] + 2\tau_c^2 \beta \rho (1 - \rho)[e^{-x} - 1 + x]$ and $x = \tau/\tau_c$. Similarly, plugging the $g_2(\tau)$ model into Eq. (3), the speckle contrast without modulation would be

$$K^2(T) = \beta \rho^2 \frac{e^{-2x} - x + 2x}{2x^2} + 4\beta\rho(1 - \rho)\frac{e^{-x} - 1 + x}{x^2} + \beta(1 - \rho)^2 + v_n \tag{14}$$

where $x = T/\tau_c$.

In simulation results presented in Fig. 2 and S5, $g_2(\tau)$ assumes the form of Eq. (12), the parameters in which are $\beta = 1$, $\rho = 1$, $v_n = 0$. T or τ ranges from 10 μs to 0.1 s with a resolution of 1 μs. The correlation time τ_c is varied in simulation.

Biomedical Optics EXPRESS

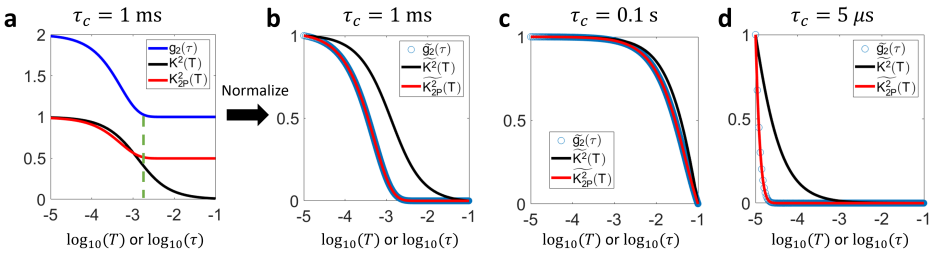

Fig. 2. Numerical simulation of K^2 and K^2_{2P} curves given the same $g_2(\tau)$. **a** Comparison of the given $g_2(\tau)$ curve with speckle contrast curves with and without 2-pulse modulation. K^2_{2P} denotes the square of 2-pulse modulated speckle contrast while K^2 represents the square of speckle contrast without within-exposure modulation. The pulse duration in 2-pulse modulation is T_m = 10 μs. τ_c = 1 ms. **b** Comparison of the three curves after separate normalization on the y-axis so that the dynamic range is all normalized to $[0, 1]$. **c** Comparison of normalized $g_2(\tau)$, $K^2(T)$ and $K^2_{2P}(T)$ when τ_c = 0.1 s. **d** Comparison of normalized $g_2(\tau)$, $K^2(T)$ and $K^2_{2P}(T)$ when τ_c = 5 μs.

2.3. Instrumentation setup

A volume holographic grating (VHG) wavelength stabilized laser diode (785 nm; LD785-SEV300, Thorlabs) is used to provide the light source. An optical isolator (Electro-Optics Technology, Inc.) based on Faraday rotation effect is placed immediately after the laser output to prevent potential inadvertent back reflections from disrupting the laser source. The light passing through the isolator is then coupled into a single-mode fiber (P3-780A-FC-2, Thorlabs, Inc.) to reshape the beam profile into a circular Gaussian one. The output beam is sent into an acousto-optic modulator (AOMO 3100-125, Gooch & Housego, Inc.) through which the power of the 1st order diffraction can be manipulated. The 0th order diffraction is filtered out by an aperture. Apart from the widefield illumination in which the output beam from AOM is deflected down and incident upon the imaging object directly, another focused illumination beam path is constructed with two convex lenses (focal length, L3: 100 mm, L4: 50 mm) whose relative distance can be adjusted to focus the beam onto the imaging spot. For detection path, the light is collected by a Nikon 24mm camera lens (AF NIKKOR 24 mm f/2.8D, Nikon, Inc.) and split into two by a 50:50 plate beamsplitter (BSW17, Thorlabs, Inc.). The transmission split is focused on a camera (acA1920-155 um, Basler, Inc.) via a Nikon 50mm lens (AF NIKKOR 50 mm f/1.8D, Nikon, Inc.). The same model of lens is used to focus the reflection split onto a fiber coupler to which a single-mode fiber (P3-780A-FC-2, Thorlabs, Inc.) is attached. The output light of the fiber is collimated via a collimator (focal length: 11 mm; F220APC-780, Thorlabs, Inc.) and focused on the photosensitive area of the APD (APD410A, Thorlabs, Inc.) by a spherical lens (focal length: 40 mm; LBF254-040-B, Thorlabs, Inc.). The intensity signal measured by APD is filtered by a low-pass filter (500 kHz; EF506, Thorlabs) and sampled by the data acquisition board at 1 MHz (USB-6363, National Instrument, Inc.).

2.4. LSCI experimental validation in vitro and in vivo

A single-channel microfluidics device is used to test the method *in vitro*. Its bulk is manufactured with polydimethylsiloxane (Dow Corning Sylgard 184 PDMS) in a 10 to 1 base-to-curing agent mixture by weight. Titanium dioxide (CAS 1317-80-2, Sigma, USA) is added into the mixture (1.8‰ w/w) to create optical properties mimicking the tissue [38]. The scattering solution flowing through the channel is made by diluting the Latex microsphere suspensions (5100A, 10% w/w, Thermo Fisher Scientific, USA) in a 4.8% v/v ratio with distilled water to mimic the optical properties of blood.

Biomedical Optics EXPRESS

The mouse cranial window preparation procedures were detailed by Kazmi et al. [39]. All animal procedures are approved by the Institutional Animal Care and Use Committee (IACUC) of University of Texas at Austin.

In 2-pulse modulated multiple-exposure imaging, 15 camera exposure times were used for demonstration of characterizing $g_2(\tau)$ at multiple time lags. $T_m = 10$ μs and T ranges from 10 μs to 5 ms. Specifically, the 15 T are 10 μs, 12 μs, 15 μs, 20 μs, 30 μs, 40 μs, 50 μs, 75 μs, 100 μs, 250 μs, 500 μs, 750 μs, 1 ms, 2.5 ms and 5 ms. The raw image size is 1000×750. Speckle contrast is computed spatially from raw images according to Eq. (2) with a 7×7 sliding window. Focused illumination is employed for both APD and camera measurements. For APD measurement, the laser power is 100 mW. In camera measurements, the laser power is attenuated by AOM to avoid pixel saturation. For *in vitro* experiements, 150 raw speckle images are collected for each camera exposure time and the raw intensity signal is recorded by APD for 10 s. The measurement is repeated 5 times for each flow rate. The flow rate increases from 0 to 100 μL/min with a step size of 10 μL/min in each repetition. The maximum and minimum ICT values in those five repetitions are discarded and the rest three are used for the ICT comparison between camera and APD measurements. For *in vivo* measurements, 30 raw camera images are collected for each exposure time and 2 s APD signal is recorded. The measurement is repeated 5 times at each point. Data collection is performed at 28 points in cranial windows of 4 mice (C57BL/6, Charles River Laboratories Inc.).

The $g_2(\tau)$ curve is calculated from APD recordings in software according to $g_2(\tau) = \frac{\langle I(t)I(t+\tau)\rangle}{\langle I\rangle^2}$ with τ equally spaced. The correlation time is extracted from $g_2(\tau)$ curve by fitting to the following model

$$g_2(\tau) = 1 + \beta[\rho e^{-(\tau/\tau_c)^n} + (1-\rho)]^2 + v_n \tag{15}$$

where β is the instrumentation factor ranging from 0 to 1, ρ denotes the fraction of dynamic component in the detected light ranging from 0 to 1, and v_n denotes the noise. n determines the type of $g_1(\tau)$ model to use. n can be fixed to 1 or chosen from 2, 1 or 0.5 based on R^2. For equally spaced τ, $g_2(\tau)$ is concentrated in the tail when $g_2(\tau)$ is plotted in the logarithmic τ scale. To counteract the skewing effects of denser $g_1(\tau)$ sampling towards larger τ in the logarithmic τ axis , weighted fitting is deployed with $1/\tau$ as the weighting function. The weighting function $w = 1/\tau$ equalizes the integral weight of data points within different τ ranges of the same length in the logarithmic scale, i.e. $\int_{e^x}^{e^{x+\Delta x}} w(\tau)d\tau \propto \Delta x$ for $\forall x \in \Re$. Weighted fitting by $1/\tau$ improves the fitting performance in the head of $g_2(\tau)$ curve (Supplemental Fig. S1). To match the τ range in 2-pulse modulated multiple-exposure speckle imaging (2PM-MESI), the $g_2(\tau)$ curve is truncated in the head such that only data of $\tau \geq 10$ μs is used for correlation time extraction.

For both focused and widefield illumination experiments, the correlation time τ_c is extracted from measured $K^2_{2P}(T)$ curves according to the following model

$$K^2_{2P}(T) = \frac{1}{2}\beta[\rho e^{-(T/\tau_c)^n} + (1-\rho)]^2 + c \tag{16}$$

where c represents a constant term independent of T. β, ρ and n have the same meaning as those in Eq. (15). T is the period of the 2-pulse modulation waveform.

3. Results

3.1. 10 μs pulse duration is short enough such that $\widetilde{K^2_{2P}}(T) = \widetilde{g_2}(T)$

In this section, we first verify the equivalency between normalized $K^2_{2P}(T)$ and $g_2(T)$ (denoted as $\widetilde{K^2_{2P}}(T)$ and $\widetilde{g_2}(T)$, respectively) with numerical simulation using a $T_m = 10$ μs pulse duration. As highlighted by the green dashed line in Fig. 2(a), the 2-pulse modulated $K^2_{2P}(T)$ decreases to the flat level earlier than the unmodulated $K^2(T)$ but at about the same time as $g_2(\tau)$. The shape of

Biomedical Optics EXPRESS

$K^2_{2P}(T)$ curve is also more similar to that of $g_2(\tau)$ compared with $K^2(T)$. Further normalization reveals the consistency between the normalized $K^2_{2P}(T)$ and $g_2(\tau)$ curves (Fig. 2(b)). Such equivalency holds for $g_2(\tau)$ curves over a wide range of decreasing speeds. The correlation time τ_c is varied from 5 μs to 0.1s, which covers the whole spectrum of τ_c reported by Postnov et al [26]. The discrepancy between $\widetilde{K^2}(T)$ and $\widetilde{g_2}(T)$ drastically increases when τ_c is reduced to 5 μs (Fig. 2(c), (d)). However, $\widetilde{K^2_{2P}}(T)$ maintains a good consistency with $\widetilde{g_2}(T)$ throughout the τ_c range (Fig. 2(c), d). The maximum relative percentage discrepancy is below 10^{-5}%.

The consistency between normalized $K^2_{2P}(T)$ and $g_2(T)$ with a 10 μs pulse duration holds experimentally as well. For *in vitro* microfluidics experiments, raw images of different exposure times under 2-pulse modulation are shown in Fig. 3(a). The average pixel intensity is approximately the same across different camera exposures, which is expected since the effective exposure time is kept the same in those exposures, i.e. all 20 μs. But the corresponding speckle contrast shows significant decrease when the temporal separation between the two illumination pulses, T, increases from 50 to 100 μs (Fig. 3(b)). Such trend is further illustrated in Fig. 3(c) where the K^2_{2P} in the microfluidic channel area decreases as T increases. In addition, K^2_{2P} of higher flow rates begins to decrease earlier than those of lower rates. Such relationship between flow rate and start time of decreasing is also reflected in $g_2(\tau)$ curves which are derived from APD measurements of 1 MHz sampling rate (Fig. 3(d)). Most importantly, When K^2_{2P} and $g_2(\tau)$ curves are normalized, they overlap on each other (Fig. 3(e)).

We noticed slight downtick in the tail of $K^2_{2P}(T)$ curves (Fig. 3(c)), which is not present in corresponding $g_2(\tau)$ curves (Fig. 3(d)). It arises from the incomplete gating of light by AOM between the two illumination pulses. When the distance between two illumination pulses, T, becomes too large relative to the pulse duration, the effects of non-zero residual illumination accumulated in between are no longer negligible and can result in a lowered $K^2_{2P}(T)$ value (Supplemental section S3). Strategies of removing the downtick will be further discussed in section 3.3. But in terms of extracting correlation times, the downtick does not seem to matter too much as results will show in the following.

Apart from comparing the values of normalized K^2_{2P} and $g_2(\tau)$, we also compared the inverse correlation time (ICT), i.e. $1/\tau_c$, extracted from $K^2_{2P}(T)$ and $g_2(\tau)$ curves. First, the electric field autocorrelation $g_1(\tau)$ model identification capability of 2-pulse modulated multiple-exposure speckle imaging (2PM-MESI) is validated against APD-based direct $g_2(\tau)$ measurements. When the flow is zero, for the best $g_1(\tau)$ model, $n = 1$. When the flow is non-zero among the tested flow rates, $n = 2$ (Supplemental Fig. S3). Second, as expected, the larger the flow rate, the larger the ICT is (Fig. 3(f)). Third, ICT extracted from $K^2_{2P}(T)$ curves consisting of only 15 values of T is consistent with that from $g_2(\tau)$ evaluated at a much denser set of τ ($R^2 = 0.99$, Fig. 3(f)). This suggests that there is redundancy in $g_2(\tau)$ curves and that the correlation time of $g_2(\tau)$ can be estimated from only a few key data points. In addition, the good consistency of ICTs between 2PM-MESI and APD based $g_2(\tau)$ measurements despite the presence of the downtick in the tails of $K^2_{2P}(T)$ curves as noted in Fig. 3(c) indicates that the fitting algorithm of correlation times is robust to slight distortion in the tails, which might be due to that the correlation time is mainly related to the decreasing region of the curve, rather than the flat region in the tail of K^2_{2P} curves.

The 2-pulse modulated $K^2_{2P}(T)$ curve is also compared with $g_2(\tau)$ *in vivo*. Figure 3(g) shows the location of three points (P1-3) where single-point direct $g_2(\tau)$ measurements are performed with an APD. Note that their vessel radii are different, i.e., P1 the largest, P2 the smallest and P3 in the middle. As expected, their $g_2(\tau)$ curves are also separated, i.e. $g_2(\tau)$ of P1 starts decreasing first while that of P2 does last (Fig. 3(h)). The normalized *in vivo* $K^2_{2P}(T)$ curve is not as consistent with that of $g_2(\tau)$ as it is *in vitro*. It could be due to the stronger flow disturbance *in vivo* as evident with the large error bars in the ICT plot (Fig. 3(i)). Note that APD and 2PM-MESI measurements are not performed simultaneously since 2PM-MESI requires modulating the

Biomedical Optics EXPRESS

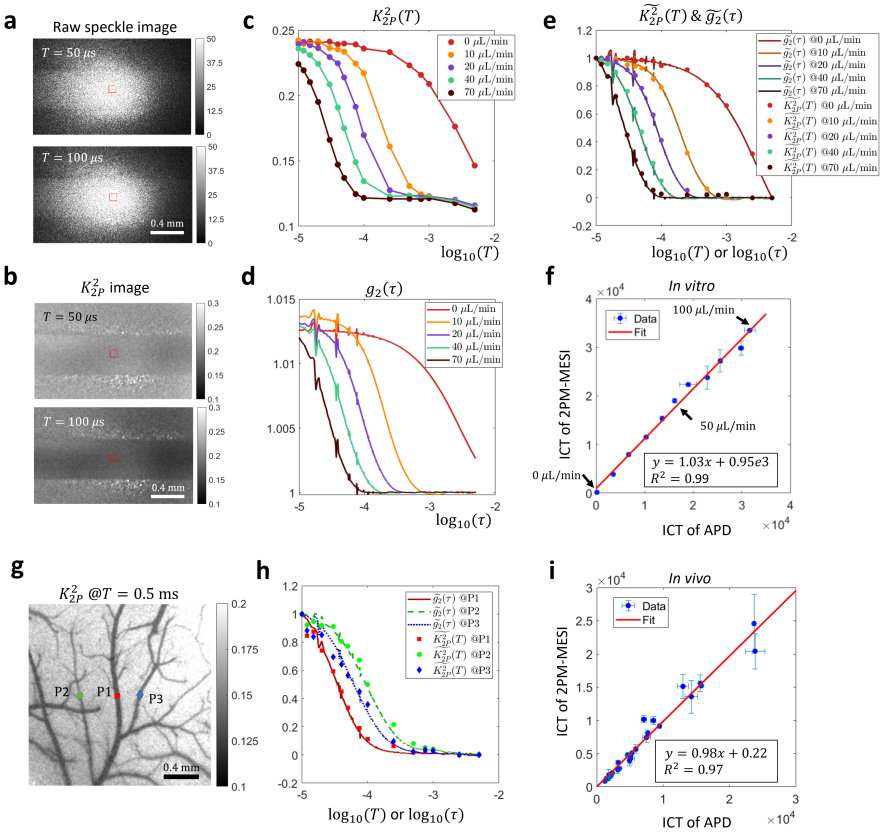

Fig. 3. Experimental validation of the consistency between normalized $K_{2P}^2(T)$ and $g_2(\tau)$ curves *in vitro* and *in vivo* under focused illumination. **a**-**f** *In vitro* microfluidic experiment results. **g**-**i** *In vivo* experiment results. **a** Raw images acquired in 2-pulse modulation strategy. **b** Speckle contrast images calculated from 2-pulse modulated raw images. **c** The $K_{2P}^2(T)$ curves extracted from the microfluidic channel region (ROI shown by red boxes in a, b) in various flow rates. **d** The $g_2(\tau)$ curves in the channel region in various flow rates. **e** Comparison of normalized $g_2(\tau)$ and normalized $K_{2P}^2(T)$. **f** Comparison of ICT values extracted from $g_2(\tau)$ and $K_{2P}^2(T)$ curves. Data points from 11 flow rates ranging from 0 to 100 μL/min with a step size of 10 μL/min are shown. The optimal $g_1(\tau)$ model is first identified by the fitting algorithm through maximizing R^2, the coefficient of determination, for both camera and APD measurements assuming three different $g_1(\tau)$ models, i.e. $g_1(\tau) = e^{-(\tau/\tau_c)^n}$ and $n = 2$, 1, or 0.5. The ICT of the optimal $g_1(\tau)$ model is then used for comparison. **g** Position of three representative points in the FOV *in vivo* where APD measurements are performed. The background K_{2P}^2 image is acquired under widefield illumination. **h** Comparison of normalized $g_2(\tau)$ and $K_{2P}^2(T)$ curves at the three points. **i** Comparison of ICT values extracted from $g_2(\tau)$ and $K_{2P}^2(T)$ curves *in vivo*. The $n = 1$ $g_1(\tau)$ model is used for curve fitting. 28 points from 4 mice are shown.

illumination while the other not. The better consistency between normalized $K_{2P}^2(T)$ and $g_2(\tau)$ *in vitro* could arise from the better flow control *in vitro*.

The $g_1(\tau)$ model identification capability is also degraded *in vivo*. ICT extracted from 2PM-MESI $K_{2P}^2(T)$ curves is consistent with that from $g_2(\tau)$ curves measured with APD when the $g_1(\tau)$ model is fixed to $n = 1$ for both APD and 2PM-MESI measurements (Fig. 3(i), $R^2 = 0.97$). Unfixing the model and let the algorithms choose the optimal n based on the

Biomedical Optics EXPRESS

fitting performance results in a degraded consistency of ICT between APD and 2PM-MESI measurements (Supplemental Fig. S4, $R^2 = 0.94$). It indicates that for complex flow dynamics *in vivo*, there is still room for the current settings of T of 2PM-MESI, e.g. the number of exposures and values of T, to be further optimized. In addition, a single $g_1(\tau)$ model might be insufficient *in vivo* and a mixed model might be warranted [26].

3.2. Widefield quasi $g_2(\tau)$ measurement and correlation time mapping

The correlation time is an important indicator of blood flow speed in LSCI. To demonstrate the 2D quasi $g_2(\tau)$ measurement and correlation time mapping capability of our method, we present in this section widefield illumination results. APD results are not shown because they are dominated by noise in this illumination regime. Figure 4(a-d) show the 2-pulse modulated quasi $g_2(\tau)$ images in wide-field illumination at various $\tau = T$. Small vessels gradually appear as T increases, indicating slower intensity fluctuations. Note that the image size is as large as 1000×750 pixels (the corresponding FOV under 2× magnification: $\sim 2.9 \times 2.2$ mm^2). Figure 4(e-g) show the inverse correlation time (ICT) maps extracted with the three different $g_1(\tau)$ models. It can be seen that the ICT map of optimal n (Fig. 4(h)) preserves the high ICT values in vascular regions in $n = 1$ and $n = 2$ ICT maps (Fig. 4(e, f)) as well as the low ICT values in parenchyma regions in $n = 0.5$ ICT map (Fig. 4(g)). In addition, the distribution of optimal n across the field of view (Fig. 4(i)) is consistent with what is reported by Postnov and Liu et al measuring $g_2(\tau)$ with high-speed cameras [26,40]. The fitting results of $K^2_{2P}(T)$ curves at three representative points

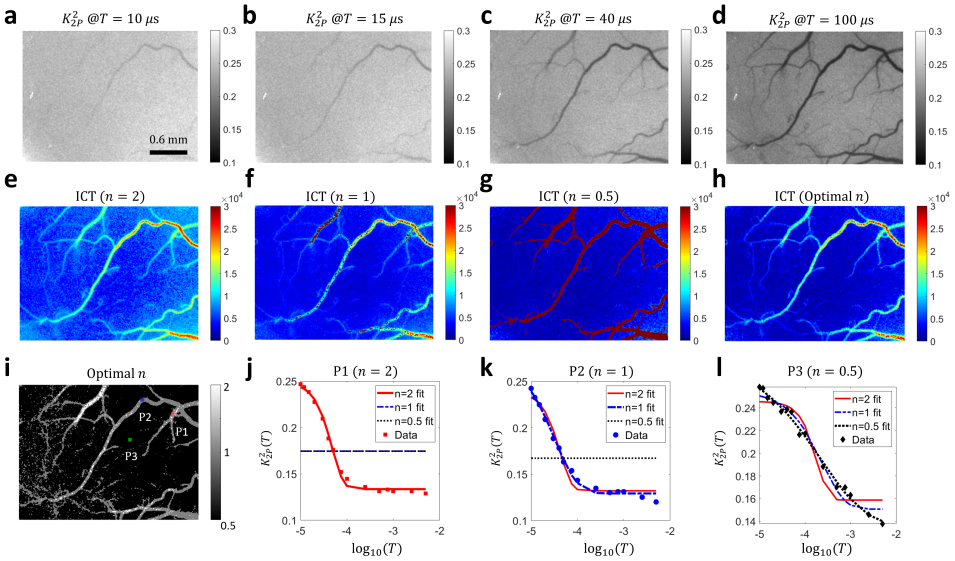

Fig. 4. 2-pulse illumination modulation across the entire field of view enables wide-field quasi $g_2(\tau)$ measurement and correlation time mapping. **a-d** The quasi $g_2(\tau)$, i.e. $K^2_{2P}(T)$ images at T = 10 μs, 15 μs, 40 μs and 100 μs, respectively. Image size: 1000×750. **e-f** ICT maps extracted with three $g_1(\tau) = e^{-(\tau/\tau_c)^n}$ models. n=2, 1 and 0.5, respectively. ICT=$1/\tau_c$. The 2D map of correlation times was obtained by fitting $K^2_{2P}(T)$ maps at 15 T time points ranging from 10 μs to 5 ms. **h** ICT map with n optimized at each pixel to maximize the R^2, the coefficient of determination. **i** Map of optimal n. **j-l** Fitting results of $K^2_{2P}(T)$ at the three points highlighted in **i**. In figure **j**, the $n = 1$ and $n = 0.5$ $g_1(\tau)$ models fail to fit the $K^2_{2P}(T)$ curve. Hence, they appear as a flat line in the plot. The same is true for the $n = 0.5$ $g_1(\tau)$ model in figure **k**.

Biomedical Optics EXPRESS

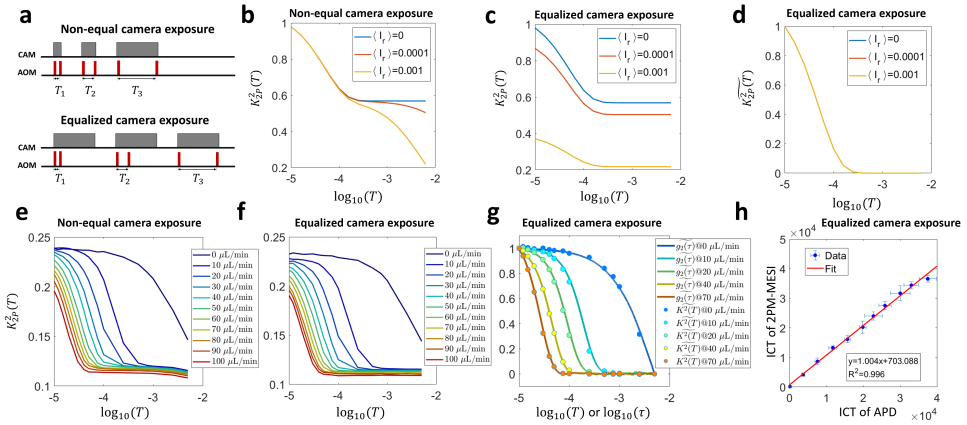

Fig. 5. Equalzing the camera exposure time eliminates the downtick of the tail of $K^2_{2P}(\tau)$ curves. **a** The diagram of the original 2-pulse modulation sequence with non-equal camera exposures and the alternative 2-pulse modulation sequence with equalized camera exposures. **b** The simulated $K^2_{2P}(T)$ curves acquired with non-equal camera exposures assuming different levels of residual light between the two illumination pulses. $\langle I_r \rangle$ denotes the ratio of the residual light's intensity over the pulsed illumination's intensity and ranges from 0 to 1. **c** The simulated $K^2_{2P}(T)$ curves acquired with equalized camera exposures assuming different levels of residual light between the two illumination pulses. **d** Normalized $K^2_{2P}(T)$ curves in equalized camera exposures. The three curves overlap, leaving only one curve visible. **e** The experimentally acquired $K^2_{2P}(T)$ curves of different flow rates using the non-equal camera exposure 2-pulse modulation sequence. **f** The experimentally acquired $K^2_{2P}(T)$ curves of different flow rates using the equalized camera exposure 2-pulse modulation sequence. **g** The plot of normalized $K^2_{2P}(T)$ curves using the equalized camera exposure vs. normalized $g_2(\tau)$ curves acquired in APD measurement. **h** The plot of ICT of 2PM-MESI with equalized camera exposures vs. that of APD measurements.

are shown in Fig. 4(j-l) (n = 2, 1 and 0.5, respectively, position shown in Fig. 4(i)). The fitting results indicate that 2PM-MESI is capable of identifying one proper $g_1(\tau)$ model according to the measured quasi $g_2(\tau)$ curve.

3.3. *Counteracting the Impact of non-zero residual illumination between two pulses*

As noted in Fig. 3(c), slight downtick would occur in the tail of $K^2_{2P}(T)$ curves. Even though the fitting algorithm seems robust in extracting the ICT values despite the presence of such slight downtick due to the incomplete gating of AOM, we would like to propose multiple solutions for correcting such downtick in the tail of $K^2_{2P}(T)$ curves. Considering that the downtick is mainly due to the incomplete gating of the AOM between the two illumination pulses, the first solution is to employ an AOM of higher contrast ratio to suppress the non-zero residual illumination between the two illumination pulses. Another approach would be to place two AOMs in the light path serially to multiply the residual light reduction. However, it increases the complexity of the instrumentation.

In addition, we would like to propose an alternative version of the 2-pulse modulation sequence which removes the downtick to increase the $g_2(\tau)$ measurement accuracy especially in the tails but with a compromised imaging speed. As shown in Fig. 5(a), different from the original non-equal exposure 2-pulse modulation sequence in which the camera exposure stops right after the second illumination pulse ends in each exposure, the alternative version of 2-pulse modulation elongates

Biomedical Optics EXPRESS

all camera exposures to the largest exposure time in the original 2-pulse modulation sequence. The AOM mediated 2-pulse illumination modulation remains the same within exposure.

Simulation results show that when the camera exposure is not equal across exposures as in the original 2-pulse modulation sequence, the downtick would occur in presence of non-zero residual light between the two illumination pulses and intensify when the amount of the residual light increases (Fig. 5(b)). However, when the camera exposure is equalized, even though the dynamic range of $K_{2P}^2(T)$ curves would shrink when the residual light increases, the tail of $K_{2P}^2(T)$ curves is always flat regardless of the residual light's level (Fig. 5(c)). In addition, when those $K_{2P}^2(T)$ curves are normalized, they co-align with that of zero residual light (Fig. 5(d)), which indicates that equalizing the camera exposure time linearly transforms the curve and preserves the correlation time compared with the zero residual light case.

Consistent with computational simulation results, the effectiveness of equalized camera exposure in counteracting the impact of non-zero residual illumination is also verified experimentally. With the same contrast ratio-limited AOM, the slight downtick induced by non-zero residual illumination in the $K_{2P}^2(T)$ curves (Fig. 5(e)) is removed by the 2-pulse modulation sequence with equalized camera exposures (Fig. 5(f)). After normalization, the $K_{2P}^2(T)$ curves in equalized camera exposures align with the APD-measured $g_2(\tau)$ curves in good consistency (Fig. 5(g)). The $g_2(\tau)$ curves here show higher signal-noise ratio than those in Fig. 3(d) thanks to improved APD shielding from environmental electromagnetic noise. The ICT extracted from the downtick-free $K_{2P}^2(T)$ curves is also consistent with that from $g_2(\tau)$ curves acquired in APD measurements (Fig. 5(h)).

4. Discussion

The intensity autocorrelation function, $g_2(\tau)$ is a fundamental tool in many optical sensing applications quantifying intensity fluctuations and investigating the light source and light-medium interaction. However, its measurement at short time lags is limited by the camera frame rate. To properly sample the rapid dynamics of intensity fluctuations, traditional two-dimensional $g_2(\tau)$ measurement methods must sacrifice either field of view or spatial resolution to increase the temporal sampling rate. We propose the 2-pulse within-exposure modulation approach to break through the camera frame limit and change the problem from fast acquisition of raw images to the fast modulation of laser illumination. We showed that the normalized $g_2(\tau)$ can be well approximated by the normalized $K_{2P}^2(T)$, the 2-pulse modulated speckle contrast. With our method, $g_2(\tau)$ can be measured at short time lags independent of camera frame rate.

The smallest time lag at which $g_2(\tau)$ can be characterized by the 2-pulse modulated multiple-exposure imaging depends on the smallest value of T that can be achieved. Since T must be greater than or equal to the pulse duration T_m, the question becomes how short the illumination pulse could be made while achieving a sufficient signal-to-noise ratio. We demonstrated that with a 10 μs pulse duration with ~100 mW laser power input into the AOM, the quasi $g_2(\tau)$ can be measured with a decent signal-to-noise ratio even in widefield illumination, which is already beyond the capability of most cameras to measure $g_2(\tau)$ with the traditional method. With a 10 μs pulse duration, we are able to evaluate quasi $g_2(\tau)$ at the smallest time lag of $\tau = 10$ μs, which would otherwise require a camera frame rate of 100 kHz with traditional methods.

A larger sampling range of τ in $g_2(\tau)$ measurement, a lower value of the lower bound of τ in particular, is significant to increasing the sensitivity to higher blood flows in LSCI. The decay of $g_2(\tau)$ is dependent on the rate of signal fluctuations. The faster the signal fluctuates and decorrelates with itself, the faster the $g_2(\tau)$ decays to the constant level. In LSCI, the speed of signal fluctuation and decorrelation is related to the blood flow. The higher the blood flow speed, the faster the signal fluctuates and decorrelates with itself, and therefore, the faster the $g_2(\tau)$ curve decays to the constant level. Therefore, measuring higher blood flow requires increasing the sampling range and capturing the $g_2(\tau)$ curve starting from shorter τ. Otherwise, the $g_2(\tau)$

Biomedical Optics EXPRESS

curve acquired would essentially be a flat curve without any meaningful decay. For this reason, we always want to measure the $g_2(\tau)$ curve starting from as short τ as possible to increase the sensitivity to high blood flows. Postnov et al. showed that the correlation times in large vessels with high blood flows in mice can be as short as 50 μs [26]. That is why they had to use a high-speed camera whose largest frame rate can be 22 kHz in reduced image size. We demonstrated 100 kHz equivalent sampling frequency using the 2-pulse modulation method. It significantly increases the $g_2(\tau)$ measurement range, which makes our method advantageous in translating into large animals or even humans in the future where the blood flow is typically higher than that in mice. Our method can adapt to situations of smaller blood flows as well by increasing the pulse duration, which can be done simply by modifying the AOM's temporal modulation sequence.

Theoretically, the measurement of $g_2(\tau)$ can be made at almost arbitrary time lags except those smaller than the pulse width T_m with the 2-pulse modulation method. The sampling of the $g_2(\tau)$ curve is determined by the number and values of the time lags. Finer sampling of the $g_2(\tau)$ curve requires more images to be acquired, but is still independent of camera frame rate. The advantage of 2-pulse modulated multiple-exposure imaging over the traditional $g_2(\tau)$ measurement method is that it enables cameras of even ordinary frame rates to measure $g_2(\tau)$ at user-specified time lags. Even though it requires the use of an AOM or similar gating hardware to modulate the illumination within the camera exposure, the overall instrumentation cost is still substantially lower than that of high-speed cameras. The camera we used costs only ~1/9 of the one used by Postnov et al [26]. Even if we consider the additional cost of AOM, the total cost is still significantly lower than that of Postnov et al.'s method. In addition, the use of pulsed illumination reduces the average power incident upon the sample compared with continuous illumination, which can reduce tissue damage or photo-bleaching of fluorophores.

In terms of the two 2-pulse modulation sequences that we proposed, i.e. non-equal camera exposure vs. equalized camera exposure, they can be selected based on case-specific needs. In cases where the accuracy of $g_2(\tau)$ measurement accuracy is prioritized and that the imaging speed is less of a concern, the equalized camera exposure modulation sequence is more suitable. In contrast, in cases where fast imaging is desired, the non-equal camera exposure modulation sequence can be a better choice. The slight downtick of tail in this case does not necessarily imply a significantly deviant correlation time estimation from the true ones as we found. If it is a concern, it can be alleviated by employing AOM of higher contrast ratio or combining two AOMs serially.

Note that we perform the modulation of the illumination, but our method is not limited to this case, especially in applications where modulation in the signal detection end is more convenient, for example intensity interferometry. In this case, modulation happens after the light interacts with the medium. Modulation could be also applied in the signal post-processing phase instead of the imaging phase.

Even though the 2-pulse modulation strategy borrows the idea of speckle contrast from LSCI, it has the potential of being generalized to other optical applications than LSCI. This is because speckle contrast is, in definition, identical to the variation coefficient of a general signal. The relationship between speckle contrast and $g_2(\tau)$ holds without special properties that would distinguish speckle from other types of intensity signal (Supplemental sections S1 and S2). Therefore, the idea of approximating $g_2(\tau)$ with speckle contrast is not necessarily limited to speckle intensity signals.

We have demonstrated the relative equivalency between $g_2(\tau)$ and 2-pulse modulated speckle contrast, i.e. $\widetilde{g_2}(T) = \widetilde{K_{2P}^2}(T)$. This is enough if we only care about the correlation time of $g_2(\tau)$ since correlation time is invariant to linear transformations of $g_2(\tau)$. However, sometimes the absolute value of $g_2(\tau)$ matters. Does our method still work in this case? We look into this question through applying 2-pulse modulation in the signal post-processing phase. According to

Biomedical Optics EXPRESS

Eq. (5), the absolute value of $g_2(\tau)$ can be estimated from 2-pulse modulated speckle contrast $K^2_{2P}(T)$, i.e. $g_2(T) = 2[K^2_{2P}(T) - C]$. As shown in Fig. 6, the $g_2(\tau)$ curves of realistic APD signals and the $2[K^2_{2P}(T) - C]$ curves calculated from the same APD signal match with each other absolutely even though not perfectly. It suggests that given the same signal collected by exactly the same instrumentation, the absolute value of $g_2(\tau)$ of the signal can be estimated from its 2-pulse modulated speckle contrast. However, to recover the absolute values of $g_2(\tau)$ accurately, the requirement on the pulse duration is higher than that to just recover the relative values (Supplemental section S4).

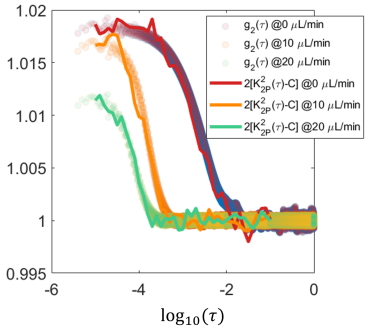

Fig. 6. Evaluating the absolute estimation of $g_2(\tau)$ based on $K^2_{2P}(T)$ through applying 2-pulse modulation in the signal post-processing phase over speckle intensity recordings. The speckle signal was acquired by APD on microfluidic devices. Temporal 2-pulse modulated speckle contrast is calculated from pixel intensities generated by gating and summing the realistic APD recordings of speckle signal.

We used very short 10 μs pulses, which might be concerning, especially *in vivo*, considering the limited light input into camera sensor. However, we would like to argue that the limited light input is a challenge not only for our method, but also for the traditional high-speed camera based $g_2(\tau)$ measurement methods. Since cameras measure the integral of the signal within the camera exposure time, to sample the signal more rapidly, the camera exposure time should be made shorter accordingly. For example, to obtain $g_2(\tau)$ at τ = 10 μs , it requires sampling the intensity signal at least every 10 μs, which means the camera exposure should be no larger than 10 μs. Even though some cameras support overlapping exposures where the next exposure can start before the last exposure ends, the camera exposure time cannot be too much longer than 10 μs since the overlapping should not be too much. Otherwise, the difference between images of neighboring exposures would be too small. Therefore, the short exposure time limits the light input and pixel intensity in high-speed cameras as well. A high-speed camera of 100 kHz cannot perform much better than our method using 10 μs pulses in terms of achieving a large average pixel intensity. In addition, we found that the pixel intensity is still reasonably large even with the 10 μs pulse duration. In focused illumination, the average pixel intensity value in the focus area *in vivo* is about 66 with 100 mW laser power input into AOM. In widefield illumination, the average pixel intensity value is lower, but it is still above 14 with the same laser power. The quality of speckle contrast images we acquire (Fig. 4(a-d)) is reasonably good. Third, the pulse duration does not have to be always as short as 10 μs. Our simulation results show that in cases of measuring $g_2(\tau)$ of large correlation times, τ_c, i.e., the $g_2(\tau)$ curve decreases slowly, the pulse duration can be extended without significantly compromising the accuracy of $g_2(\tau)$ measurement (Supplemental section 4). Last, in certain application scenarios of our method where the pixel intensity becomes significantly low, for example DCS in large animals, and that pulse duration has to be kept small, the low pixel intensity problem could be counteracted by cameras of high quantum efficiency. Since our method only requires ordinary frame rates, it is not difficult to find

Biomedical Optics EXPRESS

suitable cameras of high quantum efficiency to apply our method. In contrast, high-speed and high-quantum efficiency cameras are much more demanding and can be expected to be more expensive if we want to achieve widefield measurement of $g_2(\tau)$ using the traditional fast detector based methods in this scenario.

The 2PM-MESI transforms the research methodology on the temporal gap between two consecutive images when performing synthetic MESI. In synthetic MESI, efforts are put into minimizing the gap and avoid its negative effects on speckle contrast measurements [30,41]. However, 2PM-MESI demonstrates that such gap can be, oppositely, capitalized on to obtain valuable information about the underlying blood flow. The 2-pulse modulated images can be viewed as the superimposition of one speckle image and itself a moment later. In this case, speckle contrast of the superimposed image essentially quantifies the autocorrelation between the image and itself a moment later (Supplemental section S2). As the temporal gap in between increases, the autocorrelation decreases, and the decreasing speed is related to the probed blood flow in a profound way, which constitutes the core theoretical basis of 2PM-MESI.

Finally, compared with the traditional MESI [32], the 2-pulse modulated MESI proposed in this work represents a major improvement and upgrade to the original MESI method. It linearizes and simplifies the relation between speckle contrast and $g_2(\tau)$, which makes it possible to measure $g_2(\tau)$ directly instead of recovering it through complicated and time-consuming data post-processing like the ones used by Murali et al [42,43]. In addition, the 2 pulses of fixed duration within the camera exposure naturally equalize the average pixel intensity across exposures without illumination power adjustment, which eliminates the calibration step required in the traditional MESI to ensure that images of different exposure times have the same average pixel intensity. The imaging protocol of 2PM-MESI is simplified compared with that of the traditional MESI. The two major simplifications of 2PM-MESI over the traditional MESI make 2PM-MESI appealing in future blood flow imaging applications.

5. Conclusion

In summary, we proposed the 2-pulse modulation waveform to address the question of measuring $g_2(\tau)$ without resolving the fast temporal dynamics of the intensity signal of interest and demonstrated wide-field intensity fluctuation imaging. Under the 2-pulse modulation, the problem is essentially converted from how fast the raw intensity images can be acquired to how fast the laser illumination or the detected signal can be modulated within the camera exposure. With two modulation pulses whose duration is short enough compared with correlation times of interest, the normalized $g_2(T)$ can be approximated by the normalized $K_{2P}^2(T)$. The multiple exposures to acquire $K_{2P}^2(T)$ at different T do not need to be consecutive or acquired with a fast frame rate. It allows cameras of even ordinary frame rates to characterize the decay of intensity autocorrelation function as long as the signal's statistical property remains invariant within the measurement. The method is expected to enable the 2-dimensional measurement of quasi $g_2(\tau)$ and facilitate extracting the correlation time in wide field with a substantially lower instrumentation cost.

Funding. University of Texas at Austin (UT Austin Portugal Program); National Institutes of Health (EB011556, NS108484).

Acknowledgements. We acknowledge the support of National Institutes of Health (NIH) (Grant NS108484, EB011556) and UT Austin Portugal Program.

Author Contributions: Q. F. and A. K. D. proposed the idea and developed the theory. Q. F. designed the experiments, did the numerical simulation, *in vitro* and *in vivo* experiments. A. T performed mouse relevant operations: surgery, handling, anesthesia. Q. F., A. T. and A. K. D. wrote the manuscript together.

Disclosures. The authors declared no conflicts of interest.

Data availability. Data underlying the results presented in this paper are not publicly available at this time but may be obtained from the authors upon reasonable request.

Biomedical Optics EXPRESS

Supplemental document. See Supplement 1 for supporting content.

References

1. R. Hanbury Brown and R. Q. Twiss, "A test of a new type of stellar interferometer on sirius," Nature **178**(4541), 1046–1048 (1956).
2. W. Guerin, A. Dussaux, M. Fouché, *et al.*, "Temporal intensity interferometry: photon bunching in three bright stars," Mon. Not. R. Astron. Soc. **472**(4), 4126–4132 (2017).
3. J. Rivet, A. Siciak, E. de Almeida, *et al.*, "Intensity interferometry of p cygni in the h α emission line: towards distance calibration of lbv supergiant stars," Mon. Not. R. Astron. Soc. **494**(1), 218–227 (2020).
4. E. L. Elson and D. Magde, "Fluorescence correlation spectroscopy. i. conceptual basis and theory," Biopolymers **13**(1), 1–27 (1974).
5. D. Magde, E. L. Elson, and W. W. Webb, "Fluorescence correlation spectroscopy. ii. an experimental realization," Biopolymers **13**(1), 29–61 (1974).
6. O. Krichevsky and G. Bonnet, "Fluorescence correlation spectroscopy: the technique and its applications," Rep. Prog. Phys. **65**(2), 251–297 (2002).
7. J. Ries and P. Schwille, "Fluorescence correlation spectroscopy," BioEssays **34**(5), 361–368 (2012).
8. L. Yu, Y. Lei, Y. Ma, *et al.*, "A comprehensive review of fluorescence correlation spectroscopy," Front. Phys. **9**, 644450 (2021).
9. A. Alva, E. Brito-Alarcón, A. Linares, *et al.*, "Fluorescence fluctuation-based super-resolution microscopy: Basic concepts for an easy start," J. Microsc. **288**(3), 218–241 (2022).
10. T. Dertinger, R. Colyer, G. Iyer, *et al.*, "Fast, background-free, 3d super-resolution optical fluctuation imaging (sofi)," Proc. Natl. Acad. Sci. **106**(52), 22287–22292 (2009).
11. T. Dertinger, R. Colyer, R. Vogel, *et al.*, "Achieving increased resolution and more pixels with superresolution optical fluctuation imaging (sofi)," Opt. Express **18**(18), 18875–18885 (2010).
12. B. J. Berne and R. Pecora, *Dynamic Light Scattering: With Applications to Chemistry, Biology, and Physics* (Courier Corporation, 2000).
13. J. Stetefeld, S. A. McKenna, and T. R. Patel, "Dynamic light scattering: a practical guide and applications in biomedical sciences," Biophys. Rev. **8**(4), 409–427 (2016).
14. M. Kaszuba, D. McKnight, M. T. Connah, *et al.*, "Measuring sub nanometre sizes using dynamic light scattering," J. Nanopart. Res. **10**(5), 823–829 (2008).
15. D. A. Boas and A. G. Yodh, "Spatially varying dynamical properties of turbid media probed with diffusing temporal light correlation," J. Opt. Soc. Am. A **14**(1), 192–215 (1997).
16. T. Durduran and A. G. Yodh, "Diffuse correlation spectroscopy for non-invasive, micro-vascular cerebral blood flow measurement," NeuroImage **85**, 51–63 (2014).
17. D. A. Boas, S. Sakadžic, J. J. Selb, *et al.*, "Establishing the diffuse correlation spectroscopy signal relationship with blood flow," Neurophotonics **3**(3), 031412 (2016).
18. J. Briers and A. Fercher, "Retinal blood-flow visualization by means of laser speckle photography," Investigative Ophthalmology & Visual Science **22**(2), 255–259 (1982).
19. J. D. Briers, "Laser speckle contrast imaging for measuring blood flow," Opt. Appl. **37**(1), 1–34 (2007).
20. D. Briers, D. D. Duncan, E. R. Hirst, *et al.*, "Laser speckle contrast imaging: theoretical and practical limitations," J. Biomed. Opt. **18**(6), 066018 (2013).
21. D. A. Boas and A. K. Dunn, "Laser speckle contrast imaging in biomedical optics," J. Biomed. Opt. **15**(1), 011109 (2010).
22. A. K. Dunn, "Laser speckle contrast imaging of cerebral blood flow," Ann. Biomed. Eng. **40**(2), 367–377 (2012).
23. T. Wohland, X. Shi, J. Sankaran, *et al.*, "Single plane illumination fluorescence correlation spectroscopy (spim-fcs) probes inhomogeneous three-dimensional environments," Opt. Express **18**(10), 10627–10641 (2010).
24. J. W. Krieger, A. P. Singh, N. Bag, *et al.*, "Imaging fluorescence (cross-) correlation spectroscopy in live cells and organisms," Nat. Protoc. **10**(12), 1948–1974 (2015).
25. A. P. Singh, J. W. Krieger, J. Buchholz, *et al.*, "The performance of 2d array detectors for light sheet based fluorescence correlation spectroscopy," Opt. Express **21**(7), 8652–8668 (2013).
26. D. D. Postnov, J. Tang, S. E. Erdener, *et al.*, "Dynamic light scattering imaging," Sci. Adv. **6**(45), eabc4628 (2020).
27. Y. Yuan, Y. Bi, X. C. Gao, *et al.*, "High-dynamic-range blood flow rate measurement in a large-diameter vessel," Appl. Opt. **60**(23), 6837–6842 (2021).
28. C. P. Valdes, H. M. Varma, A. K. Kristoffersen, *et al.*, "Speckle contrast optical spectroscopy, a non-invasive, diffuse optical method for measuring microvascular blood flow in tissue," Biomed. Opt. Express **5**(8), 2769–2784 (2014).
29. T. Dragojević, D. Bronzi, H. M. Varma, *et al.*, "High-speed multi-exposure laser speckle contrast imaging with a single-photon counting camera," Biomed. Opt. Express **6**(8), 2865–2876 (2015).
30. T. Dragojević, J. L. Hollmann, D. Tamborini, *et al.*, "Compact, multi-exposure speckle contrast optical spectroscopy (scos) device for measuring deep tissue blood flow," Biomed. Opt. Express **9**(1), 322–334 (2018).
31. C. Yi, J. Jung, J. Im, *et al.*, "Single-shot temporal speckle correlation imaging using rolling shutter image sensors," Optica **9**(11), 1227–1237 (2022).
32. A. B. Parthasarathy, W. J. Tom, A. Gopal, *et al.*, "Robust flow measurement with multi-exposure speckle imaging," Opt. Express **16**(3), 1975–1989 (2008).

Biomedical Optics EXPRESS

33. S. M. S. Kazmi, A. B. Parthasarthy, N. E. Song, *et al.*, "Chronic imaging of cortical blood flow using multi-exposure speckle imaging," J. Cereb. Blood Flow & Metab. **33**(6), 798–808 (2013).
34. S. S. Kazmi, S. Balial, and A. K. Dunn, "Optimization of camera exposure durations for multi-exposure speckle imaging of the microcirculation," Biomed. Opt. Express **5**(7), 2157–2171 (2014).
35. C. Smith, A. Santorelli, S. Engelmann, *et al.*, "All fiber-based illumination system for multi-exposure speckle imaging," Biomed. Opt. Express **14**(2), 771–782 (2023).
36. R. Bandyopadhyay, A. Gittings, S. Suh, *et al.*, "Speckle-visibility spectroscopy: A tool to study time-varying dynamics," Rev. Sci. Instrum. **76**(9), 093110 (2005).
37. M. Siket, I. Jánoki, K. Demeter, *et al.*, "Time varied illumination laser speckle contrast imaging," Opt. Lett. **46**(4), 713–716 (2021).
38. C. T. Sullender, A. Santorelli, L. M. Richards, *et al.*, "Using pressure-driven flow systems to evaluate laser speckle contrast imaging," J. Biomed. Opt. **28**(03), 036003 (2023).
39. S. S. Kazmi, E. Faraji, M. A. Davis, *et al.*, "Flux or speed? examining speckle contrast imaging of vascular flows," Biomed. Opt. Express **6**(7), 2588–2608 (2015).
40. C. Liu, K. Kiliç, S. E. Erdener, *et al.*, "Choosing a model for laser speckle contrast imaging," Biomed. Opt. Express **12**(6), 3571–3583 (2021).
41. M. Chammas and F. Pain, "Synthetic exposure with a cmos camera for multiple exposure speckle imaging of blood flow," Sci. Rep. **12**(1), 4708 (2022).
42. K. Murali, A. Nandakumaran, T. Durduran, *et al.*, "Recovery of the diffuse correlation spectroscopy data-type from speckle contrast measurements: towards low-cost, deep-tissue blood flow measurements," Biomed. Opt. Express **10**(10), 5395–5413 (2019).
43. K. Murali, A. Nandakumaran, and H. M. Varma, "On the equivalence of speckle contrast-based and diffuse correlation spectroscopy methods in measuring in vivo blood flow," Opt. Lett. **45**(14), 3993–3996 (2020).